Postbuckling of carbon nanotube-reinforced functionally graded cylindrical panels under axial compression using a meshless approach

K.M. Liew [a,*], Z.X. Lei [a,b], J.L. Yu [b], L.W. Zhang [c]

[a] Department of Civil and Architectural Engineering, City University of Hong Kong, Kowloon, Hong Kong
[b] CAS Key Laboratory of Mechanical Behavior and Design of Materials, University of Science and Technology of China, PR China
[c] College of Information Technology, Shanghai Ocean University, 999 Huchenghuan Road, Shanghai 201306, PR China

ARTICLE INFO

ABSTRACT

This paper presents a postbuckling analysis of carbon nanotube-reinforced functionally graded (CNTR-FG) cylindrical panels under axial compression. Based on kernel particle approximations for the field variables, the Ritz method is employed to obtain the discretized governing equations. The cylindrical panels are reinforced by single-walled carbon nanotubes (SWCNTs) which are assumed to be graded through the thickness direction with different types of distributions. The effective material properties of CNTR-FG cylindrical panels are estimated through a micromechanical model based on the extended rule of mixture. To eliminate shear locking for a very thin cylindrical panel, the system's bending stiffness is evaluated by a stabilized conforming nodal integration scheme and the membrane as well as shear terms are calculated by the direct nodal integration method. In the present study, the arc-length method combined with the modified Newton–Raphson method is used to trace the postbuckling path. Detailed parametric studies are carried out to investigate effects of various parameters on postbuckling behaviors of CNTR-FG cylindrical panels and results for uniformly distributed (UD) CNTR-FG cylindrical panel are provided for comparison.

1. Introduction

Carbon nanotube-reinforced composite (CNTRC) material, known as the replacement for conventional carbon fibers with carbon nanotubes (CNTs), has drawn considerable attention from researchers in many engineering fields [1–3]. CNTs have been demonstrated to have high strength and stiffness with high aspect ratio and low density. Considering these remarkable properties, CNTs can be selected as an excellent candidate for reinforcement of polymer composites. Sun et al. [4] analytically investigated the axial Young's modulus of single-walled carbon nanotube (SWCNT) arrays with diameters ranging from nanometer to meter scales. Their results confirmed that CNTs have mechanical properties superior than carbon fibers.

In recent years, many works have been carried out to study the constitutive models and mechanical properties of CNT polymer composites. Coleman et al. [5] reported a review and comparison of mechanical properties of CNTRCs fabricated by different processing methods. Tensile tests of CNT composites have demonstrated that reinforcement with only 1 wt%

* Corresponding author. Tel.: +852 34426581.
  E-mail address: kmliew@cityu.edu.hk (K.M. Liew).

nanotubes resulted in 36–42% increase in elastic modulus and 25% increase in break stress [6]. Gojny et al. [7] investigated the influence of different types of nanofillers on mechanical properties of epoxy-based nanocomposites and the relevance of surface functionalisation. They discovered that the strength and stiffness of the nanocomposites produced can be considerably enhanced and a significant increase in fracture toughness was also observed. Pötschke et al. [8] studied rheological behavior of compression molded mixtures of polycarbonate and carbon nanotubes using oscillatory rheometry at 260 °C. They discovered that 2 wt% nanotubes caused an obvious improvement in electrical resistivity and complex viscosity. The thermo-mechanical properties of epoxy-based nanocomposites reinforced by randomly oriented single- and multi-walled CNTs were examined by Fidelus et al. [9]. These investigations indicated that the introduction of CNTs into a polymer matrix may greatly improve mechanical, electrical and thermal properties of the resulting nanocomposites.

Since structure elements (beam, plate and shell) are widely used in actual structural applications, it is necessary to obtain global responses of CNTRCs in actual structure elements. Wuite and Adali [10] presented a multiscale analysis of deflection and stress behavior of CNTRC beams and a pure bending and bending-induced buckling analysis of a nanocomposite beam was reported by Vodenitcharova and Zhang [11]. Yas and Samadi [12] studied free vibration and buckling of nanocomposite Timoshenko beams reinforced by SWCNTs resting on an elastic foundation. By using the finite element method (FEM) based on the first order shear deformation plate theory, Zhu et al. [13] carried out bending and free vibration analyses of functionally graded CNTRC plates. Shen [14] presented an analysis of nonlinear bending of functionally graded CNTRC plates in thermal environments using a two step perturbation technique. Based on a higher-order shear deformation plate theory, the large amplitude vibration of nanocomposite plates reinforced by SWCNTs resting on an elastic foundation in thermal environments was investigated by Wang and Shen [15]. Effective material properties estimated by either the Eshelby–Mori–Tanaka approach or the extended rule of mixture were used for investigating the impact of uniaxial and biaxial in-plane loadings on a functionally graded nanocomposite rectangular plate [16]. In addition to analysis of beams and plates, much research has been done about CNTRC cylindrical shells. Shen and Xiang [17] examined the large amplitude vibration behavior of nanocomposite cylindrical shells in thermal environments. Aragh et al. [18] studied natural frequency characteristics of a continuously graded CNT-reinforced cylindrical panel based on the Eshelby–Mori–Tanaka approach. Based on the multiscale approach, numerical simulations were carried out for thermal buckling and postbuckling analysis of nanocomposite cylindrical shells subjected to a uniform temperature rise [19]. For nanocomposite cylindrical shells subjected to axial and pressure loads, a postbuckling analysis was also conducted by Shen in [20,21].

The main purpose of the present work is to investigate the postbuckling behaviors of carbon nanotube-reinforced functionally graded (CNTR-FG) cylindrical panels under axial compression. The element-free *kp*-Ritz method previously used for plate problems [22,23] is now extended to study CNTR-FG cylindrical panel problems. In this study, the element-free *kp*-Ritz method based on the first-order shear deformation shell theory is adopted to derive the discretized governing equations which are solved by a combination of the arc-length iterative algorithm and the modified Newton–Raphson method, to trace the postbuckling path. In this paper, several different types of distributions of single-walled carbon nanotubes (SWCNTs) in the thickness direction are considered. The effective material properties of CNTR-FG cylindrical panels are estimated through a micromechanical model based on the extended rule of mixture. In computational simulation, several numerical examples are presented to investigate the influences of carbon nanotube volume fraction, length-to-thickness ratio and radius on the postbuckling behavior of CNTR-FG cylindrical panels. The effects of boundary condition and distribution type of CNTs are also examined in detail.

2. Carbon nanotube-reinforced composite cylindrical panels

As shown in Fig. 1, three types of CNTR-FG cylindrical panels (UD, FG-O and FG-X) with length a, radius R, span angle θ_0 and thickness h are considered in this paper. The CNTs are assumed uniaxially aligned in the axial direction of the cylindrical panels, that is, UD represents uniformly distributed; FG-O and FG-X denote the other two types of functionally graded distributions of CNTs which are symmetric about the middle surface of the cylindrical panel. For FG-O type panel, the middle surface of the cylindrical panel is CNT-rich and in case of FG-X, both top and bottom surfaces are CNT-rich. As it is well described that the structure of CNT extensively affects the effective material properties of CNT-reinforced materials [24–27], several micromechanical models have been successfully developed to predict the effective material properties of CNT-reinforced nanocomposites, such as Eshelby–Mori–Tanaka scheme [28–30] and the extended rule of mixture [14,31]. Compared with the Mori–Tanaka scheme applicable to microparticles, the rule of mixture is simple and convenient to obtain the overall material properties and responses of the CNTR-FG structures. In [32], the accuracy of the rule of mixture was discussed and an excellent agreement was reported between the Mori–Tanaka and Voigt models for functionally graded ceramic–metal beams. The effective material properties of CNTR-FG cylindrical panels are given according to [14]:

$$E_{11} = \eta_1 V_{CNT} E_{11}^{CNT} + V_m E^m, \tag{1}$$

$$\frac{\eta_2}{E_{22}} = \frac{V_{CNT}}{E_{22}^{CNT}} + \frac{V_m}{E^m}, \tag{2}$$
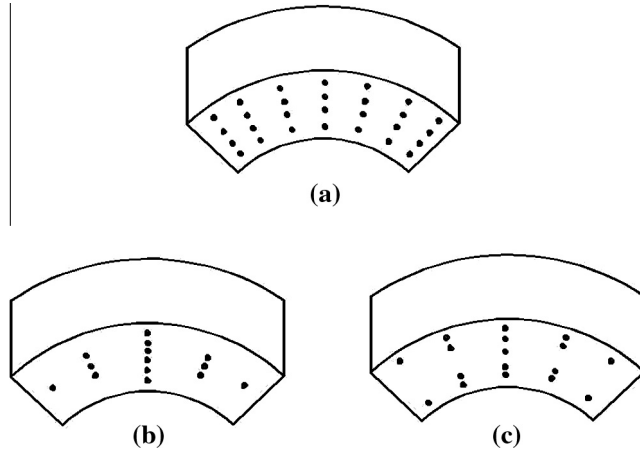
Fig. 1. Carbon nanotube reinforced composite cylindrical panels. (a) UD CNTRC cylindrical panel; (b) FG-O CNTRC cylindrical panel; (c) FG-X CNTRC cylindrical panel.

$$\frac{\eta_3}{G_{12}} = \frac{V_{CNT}}{G_{12}^{CNT}} + \frac{V_m}{G^m}, \tag{3}$$

where E_{11}^{CNT}, E_{22}^{CNT} and E^m are the Young's moduli of CNTs and the matrix, respectively. G_{12}^{CNT} and G^m are the shear moduli. With the knowledge that the load transfer between the nanotube and polymeric phases is less than perfect (e.g. the surface effects, strain gradients effects, intermolecular coupled stress effects, etc.), η_j $(j = 1, 2, 3)$, which are CNT efficiency parameters, are introduced in Eqs. (1)–(3) to consider the size-dependent material properties. Through matching the elastic moduli predicted by the MD simulations with the solutions of the extended rule of mixture in Eqs. (1)–(3), the values of η_j will be determined later.

Moreover, V_{CNT} and V_m are volume fractions of CNTs and the matrix, related by

$$V_{CNT} + V_m = 1. \tag{4}$$

According to distributions of CNTs in the thickness direction of cylindrical panels, CNT volume fractions $V_{CNT}(z)$ of various types of CNTR-FG cylindrical panels can be expressed as

$$V_{CNT}(z) = \begin{cases} V_{CNT}^* & \text{(UD)}, \\ 2\left(1 - \frac{2|z|}{h}\right)V_{CNT}^* & \text{(FG-O)}, \\ 2\left(\frac{2|z|}{h}\right)V_{CNT}^* & \text{(FG-X)}, \end{cases} \tag{5}$$

where

$$V_{CNT}^* = \frac{w_{CNT}}{w_{CNT} + (\rho^{CNT}/\rho^m) - (\rho^{CNT}/\rho^m)w_{CNT}}, \tag{6}$$

in which w_{CNT} is the mass fraction of CNTs, and ρ_m and ρ^{CNT} are densities of the matrix and CNTs, respectively. The overall CNT volume fractions of UD cylindrical panel and those of the other two types of CNTR-FG cylindrical panels are similar, which means these three types CNTR-FG cylindrical panels having the same mass and volume of CNTs.

As Poisson's ratio is not sensitive to position, ν_{12} is assumed as

$$\nu_{12} = V_{CNT}^* \nu_{12}^{CNT} + V_m \nu^m, \tag{7}$$

where ν_{12}^{CNT} and ν^m are Poisson's ratios of CNTs and matrix, respectively.

Similarly, the thermal expansion coefficients can be calculated by

$$\alpha_{11} = V_{CNT} \alpha_{11}^{CNT} + V_m \alpha^m, \tag{8}$$

$$\alpha_{22} = \left(1 + \nu_{12}^{CNT}\right)V_{CNT}\alpha_{22}^{CNT} + (1 + \nu^m)V_m\alpha^m - \nu_{12}\alpha_{11}, \tag{9}$$

where α_{11}^{CNT} and α_{22}^{CNT} are thermal expansion coefficients of CNTs. α^m is the expansion coefficient of the matrix. Since it is assumed that material properties of CNTs and matrix are temperature-dependent, the resulting material properties of CNTR-FG cylindrical panels, such as Young's modulus, shear modulus and thermal expansion coefficients, are functions of temperature and position.

3. Theoretical formulations

3.1. Total potential energy

According to the first-order shear deformation shell theory [33], displacements (u, v, w) at points (x, y, z) in the panels are expressed as functions of displacements and rotations of the middle surface of the cylindrical panel:

$$u(x,y,z) = u_0(x,y) + z\phi_x(x,y),$$ (10)

$$v(x,y,z) = v_0(x,y) + z\phi_y(x,y),$$ (11)

$$w(x,y,z) = w_0(x,y),$$ (12)

where u, v and w are the displacements along the x, y and z directions, and $(u_0, v_0, w_0, \phi_x, \phi_y)$ are the displacement components on the mid-plane ($z = 0$). It is worth noting that

$$\phi_x = \frac{\partial u}{\partial z}, \quad \phi_y = \frac{\partial v}{\partial z},$$ (13)

which indicate that ϕ_x and ϕ_y are the transverse normal rotations about the positive y and negative x axes, respectively.

With von Kármán's assumptions for moderately large deformation, the strain components can be written as

$$\begin{Bmatrix} \varepsilon_{xx} \\ \varepsilon_{yy} \\ \gamma_{xy} \end{Bmatrix} = \boldsymbol{\varepsilon}_0 + z\boldsymbol{\kappa} = \begin{Bmatrix} \frac{\partial u_0}{\partial x} + \frac{1}{2}\left(\frac{\partial w_0}{\partial x}\right)^2 \\ \frac{\partial v_0}{\partial y} + \frac{w_0}{R} + \frac{1}{2}\left(\frac{\partial w_0}{\partial y}\right)^2 \\ \frac{\partial u_0}{\partial y} + \frac{\partial v_0}{\partial x} + \frac{\partial w_0}{\partial x}\frac{\partial w_0}{\partial y} \end{Bmatrix} + z\begin{Bmatrix} \frac{\partial \phi_x}{\partial x} \\ \frac{\partial \phi_y}{\partial y} \\ \frac{\partial \phi_x}{\partial y} + \frac{\partial \phi_y}{\partial x} \end{Bmatrix},$$ (14)

$$\begin{Bmatrix} \gamma_{yz} \\ \gamma_{xz} \end{Bmatrix} = \boldsymbol{\gamma}_0 = \begin{Bmatrix} \phi_y + \frac{\partial w_0}{\partial y} - \frac{v_0}{R} \\ \phi_x + \frac{\partial w_0}{\partial x} \end{Bmatrix}.$$ (15)

The total in-plane force resultants, total moment resultants, transverse shear force resultants and thermal stress resultants are expressed as

$$\begin{Bmatrix} \mathbf{N} \\ \mathbf{M} \\ \mathbf{Q}s \end{Bmatrix} = \begin{bmatrix} \mathbf{A} & \bar{\mathbf{B}} & 0 \\ \bar{\mathbf{B}} & \mathbf{D} & 0 \\ 0 & 0 & \mathbf{A}^s \end{bmatrix} \begin{Bmatrix} \boldsymbol{\varepsilon}_0 \\ \boldsymbol{\kappa} \\ \boldsymbol{\gamma}_0 \end{Bmatrix} - \begin{Bmatrix} \mathbf{N}^T \\ \mathbf{M}^T \\ 0 \end{Bmatrix}$$ (16)

where matrixes $\mathbf{A}$, $\mathbf{B}$, $\mathbf{D}$ and $\mathbf{A}^s$ are in-plane extensional, bending-extensional coupling, bending and shear stiffness, respectively [33]. $\mathbf{N}^T$ and $\mathbf{M}^T$ are the thermal force and moment resultants, defined as

$$\mathbf{N}^T = \int_{-h/2}^{h/2} [\alpha_{11} \quad \alpha_{22} \quad 0](Q_{11} + Q_{12})\Delta T dz$$ (17)

$$\mathbf{M}^T = \int_{-h/2}^{h/2} [\alpha_{11} \quad \alpha_{22} \quad 0](Q_{11} + Q_{12})\Delta T z dz$$ (18)

The strain energy of the CNTRC cylindrical panel is given as

$$U_\varepsilon = \frac{1}{2}\int_\Omega \boldsymbol{\varepsilon}^T \mathbf{S}\boldsymbol{\varepsilon} d\Omega,$$ (19)

where

$$\boldsymbol{\varepsilon} = \begin{Bmatrix} \boldsymbol{\varepsilon}_0 \\ \boldsymbol{\kappa} \\ \boldsymbol{\gamma}_0 \end{Bmatrix}, \quad \mathbf{S} = \begin{bmatrix} \mathbf{A} & \bar{\mathbf{B}} & \mathbf{0} \\ \bar{\mathbf{B}} & \mathbf{D} & \mathbf{0} \\ \mathbf{0} & \mathbf{0} & \mathbf{A}^s \end{bmatrix}.$$ (20)

The external work is given by

$$W_e = \int_\Omega \mathbf{u}^T \bar{\mathbf{f}} d\Omega + \int_\Gamma \mathbf{u}^T \bar{\mathbf{t}} d\Gamma,$$ (21)

where $\bar{\mathbf{f}}$ represents the external load and $\bar{\mathbf{t}}$ is the prescribed traction on the natural boundary.

Eventually, the total potential energy functional of the CNTR-FG cylindrical panel can be expressed as

$$\Pi_s = U_\varepsilon - W_e.$$ (22)

3.2. Discrete system equations

In this section, the construction of shape functions for reproducing kernel particle method is briefly reviewed. For a cylindrical panel domain, the generic displacement field can be expressed as

$$(u, v, w, \phi_x, \phi_y)^T = \sum_{I=1}^{NP} \psi_I(\boldsymbol{x})(u_I, v_I, w_I, \phi_{xI}, \phi_{yI})^T = \sum_{I=1}^{NP} \psi_I(\boldsymbol{x})\mathbf{u}_I, \tag{23}$$

where $\psi_I(\boldsymbol{x})$ and $\mathbf{u}_I$ are the shape function and nodal parameter associated with node I, respectively, and NP is the number of scattered nodes. In reproducing kernel particle method [34,35], the two-dimensional shape functions are defined as

$$\psi_I(\boldsymbol{x}) = C(\boldsymbol{x}; \boldsymbol{x} - \boldsymbol{x}_I)\Phi_a(\boldsymbol{x} - \boldsymbol{x}_I), \tag{24}$$

where $\Phi_a(\boldsymbol{x} - \boldsymbol{x}_I)$ is the kernel function and $C(\boldsymbol{x}; \boldsymbol{x} - \boldsymbol{x}_I)$ is the correction function introduced to satisfy reproducing conditions

$$\sum_{I=1}^{NP} \psi_I(\boldsymbol{x})x_I^p y_I^q = x^p y^q \quad \text{for } p + q = 0, 1, 2. \tag{25}$$

$$C(\boldsymbol{x}; \boldsymbol{x} - \boldsymbol{x}_I) = \mathbf{H}^T(\boldsymbol{x} - \boldsymbol{x}_I)\mathbf{b}(\boldsymbol{x}), \tag{26}$$

where

$$\mathbf{b}(\boldsymbol{x}) = [b_0(x,y), b_1(x,y), b_2(x,y), b_3(x,y), b_4(x,y), b_5(x,y)]^T, \tag{27}$$

$$\mathbf{H}^T(\boldsymbol{x} - \boldsymbol{x}_I) = [1, x - x_I, y - y_I, (x - x_I)(y - y_I), (x - x_I)^2, (y - y_I)^2], \tag{28}$$

Now, the shape function can be written as

$$\psi_I(\boldsymbol{x}) = \mathbf{b}^T(\boldsymbol{x})\mathbf{H}(\boldsymbol{x} - \boldsymbol{x}_I)\Phi_a(\boldsymbol{x} - \boldsymbol{x}_I), \tag{29}$$

Substituting Eq. (29) into reproduction condition leads to

$$\mathbf{b}(\boldsymbol{x}) = \mathbf{M}^{-1}(\boldsymbol{x})\mathbf{H}(\mathbf{0}), \tag{30}$$

where

$$\mathbf{M}(\boldsymbol{x}) = \sum_{I=1}^{NP} \mathbf{H}(\boldsymbol{x} - \boldsymbol{x}_I)\mathbf{H}^T(\boldsymbol{x} - \boldsymbol{x}_I)\Phi_a(\boldsymbol{x} - \boldsymbol{x}_I), \tag{31}$$

$$\mathbf{H}(\mathbf{0}) = [1, 0, 0, 0, 0, 0,]^T, \tag{32}$$

The two-dimensional kernel function $\Phi_a(\boldsymbol{x} - \boldsymbol{x}_I)$ is defined as

$$\Phi_a(\boldsymbol{x} - \boldsymbol{x}_I) = \Phi_a(x) \cdot \Phi_a(y), \tag{33}$$

where

$$\Phi_a(x) = \varphi\left(\frac{x - x_I}{a}\right). \tag{34}$$

The cubic spline function is used here as the weight function $\varphi(x)$

$$\varphi_z(z_I) = \begin{cases} \frac{2}{3} - 4z_I^2 + 4z_I^3 & \text{for } 0 \leq |z_I| \leq \frac{1}{2} \\ \frac{4}{3} - 4z_I + 4z_I^2 - \frac{4}{3}z_I^3 & \text{for } \frac{1}{2} < |z_I| \leq 1 \\ 0 & \text{otherwise} \end{cases}, \tag{35}$$

where

$$z_I = \frac{x - x_I}{d_I}, \quad d_I = d_{\max}c_I, \tag{36}$$

where d_I is the size of the support of node I. $d_{\max}$ is a scaling factor and distance c_I is chosen by searching a sufficient number of nodes to avoid the singularity of matrix $\mathbf{M}$.

The shape function can be expressed as

$$\psi_I(\boldsymbol{x}) = \mathbf{H}^T(\mathbf{0})\mathbf{M}^{-1}(\boldsymbol{x})\mathbf{H}(\boldsymbol{x} - \boldsymbol{x}_I)\Phi_a(\boldsymbol{x} - \boldsymbol{x}_I). \tag{37}$$

Since the present shape function $\psi_I(\boldsymbol{x})$ does not possess Kronecker delta property, the transformation method [34] is employed to impose the essential boundary conditions in this paper.

Substituting Eq. (23) into (22) and taking the variation of the total potential energy functional lead to the discrete system equation

$$\mathbf{K}_s(\mathbf{u})\mathbf{u} = \mathbf{F}, \tag{38}$$

where

$$\mathbf{K}_s(\mathbf{u}) = \mathbf{K}^L + \mathbf{K}^N(\mathbf{u}), \tag{39}$$

$$\mathbf{F}_I = \int_\Omega \psi_I \bar{\mathbf{f}} d\Omega + \int_\Gamma \psi_I \bar{t} d\Gamma + \int_\Omega \left[\mathbf{B}_I^{m^T} \quad \mathbf{B}_I^{b^T} \right] \begin{bmatrix} \mathbf{N}^T \\ \mathbf{M}^T \end{bmatrix} d\Omega, \tag{40}$$

where $\mathbf{K}^L$ and $\mathbf{K}^N(\mathbf{u})$ represent the linear and nonlinear parts of the stiffness matrix, respectively, and are given by

$$\mathbf{K}^L = \mathbf{K}^b + \mathbf{K}^m + \mathbf{K}^s + \mathbf{K}^t, \tag{41}$$

$$\mathbf{K}_{IJ}^b = \int_\Omega \mathbf{B}_I^{b^T} \mathbf{D} \mathbf{B}_J^b d\Omega, \tag{42}$$

$$\mathbf{K}_{IJ}^m = \int_\Omega \mathbf{B}_I^{m^T} \mathbf{A} \mathbf{B}_J^m d\Omega + \int_\Omega \mathbf{B}_I^{m^T} \bar{\mathbf{B}} \mathbf{B}_J^b d\Omega + \int_\Omega \mathbf{B}_I^{b^T} \bar{\mathbf{B}} \mathbf{B}_J^m d\Omega, \tag{43}$$

$$\mathbf{K}_{IJ}^s = \int_\Omega \mathbf{B}_I^{s^T} \mathbf{A}^s \mathbf{B}_J^s d\Omega, \tag{44}$$

$$\mathbf{K}^t = \int_\Omega \bar{\mathbf{G}}_I^T \bar{\mathbf{N}} \bar{\mathbf{G}}_J d\Omega, \tag{45}$$

$$\mathbf{K}_{IJ}^N = \int_\Omega \left(\frac{1}{2} \mathbf{B}_I^{L^T} S \mathbf{B}_J^N + \mathbf{B}_I^{N^T} S \mathbf{B}_J^L + \frac{1}{2} \mathbf{B}_I^{N^T} S \mathbf{B}_J^N \right) d\Omega. \tag{46}$$

$$\mathbf{B}_I^L = \begin{bmatrix} \mathbf{B}_I^m \\ \mathbf{B}_I^b \\ \mathbf{B}_I^s \end{bmatrix}, \mathbf{B}_I^N = \bar{\mathbf{H}} \bar{\mathbf{G}}. \tag{47}$$

The bending stiffness matrices $\mathbf{K}^b$ are evaluated via the stabilized nodal integration [36] and the other stiffness and force terms $\mathbf{K}^m$, $\mathbf{K}^s$, $\mathbf{K}^t$, $\mathbf{K}^N$ and $\mathbf{F}_I$ are calculated using direct nodal integration [37] instead of the Gauss integration since the stabilized nodal integration and direct nodal integration may reduce the high computational cost and eliminate errors caused by the mismatch between the quadrature cells and the shape function supports [38]. Approximations of Eqs. (40) and (42)–(46) are given by

$$\mathbf{K}_{IJ}^b = \sum_{L=1}^{NP} \tilde{\mathbf{B}}_I^{b^T}(x_L) \mathbf{D} \tilde{\mathbf{B}}_J^b(\mathbf{x}_L) A_L, \tag{48}$$

$$\mathbf{K}_{IJ}^m = \sum_{L=1}^{NP} \left[\mathbf{B}_I^{m^T}(\mathbf{x}_L) \mathbf{A} \mathbf{B}_J^m(\mathbf{x}_L) + \mathbf{B}_I^{m^T}(\mathbf{x}_L) \bar{\mathbf{B}} \mathbf{B}_J^b(\mathbf{x}_L) + \mathbf{B}_I^{b^T}(\mathbf{x}_L) \bar{\mathbf{B}} \mathbf{B}_J^m(\mathbf{x}_L) \right] A_L, \tag{49}$$

$$\mathbf{K}_{IJ}^s = \sum_{L=1}^{NP} \mathbf{B}_I^{s^T}(\mathbf{x}_L) \mathbf{A}^s \mathbf{B}_J^s(\mathbf{x}_L) A_L, \tag{50}$$

$$\mathbf{K}^t = \sum_{L=1}^{NP} \bar{\mathbf{G}}_I^T(\mathbf{x}_L) \bar{\mathbf{N}} \bar{\mathbf{G}}_J(\mathbf{x}_L) A_L, \tag{51}$$

$$\mathbf{K}_{IJ}^N = \sum_{L=1}^{NP} \left[\frac{1}{2} \mathbf{B}_I^{L^T}(\mathbf{x}_L) S \mathbf{B}_J^N(\mathbf{x}_L) + \mathbf{B}_I^{N^T}(\mathbf{x}_L) S \mathbf{B}_J^L(\mathbf{x}_L) + \frac{1}{2} \mathbf{B}_I^{N^T}(\mathbf{x}_L) S \mathbf{B}_J^N(\mathbf{x}_L) \right] A_L, \tag{52}$$

$$\mathbf{F}_I = \sum_{L=1}^{NP} \psi_I(\mathbf{x}_L) \bar{\mathbf{f}}(\mathbf{x}_L) A_L + \sum_{L=1}^{NPb} \psi_I(\mathbf{x}_L) \bar{\mathbf{t}}(\mathbf{x}_L) s_L + \sum_{L=1}^{NP} \left[\mathbf{B}_I^{m^T}(\mathbf{x}_L) \quad \mathbf{B}_I^{b^T}(\mathbf{x}_L) \right] \begin{bmatrix} \mathbf{N}^T \\ \mathbf{M}^T \end{bmatrix} A_L, \tag{53}$$

where $\mathbf{x}_L$ and A_L are the nodal coordinate and representative area, respectively; NP and s_L denote the number of nodes on the natural boundary and the weights associated with the boundary point, respectively. Here matrices $\tilde{\mathbf{B}}_I^b(\mathbf{x}_L)$, $\mathbf{B}_I^b(\mathbf{x}_L)$, $\mathbf{B}_I^m(\mathbf{x}_L)$, $\mathbf{B}_I^s(\mathbf{x}_L)$, $\bar{\mathbf{G}}(\mathbf{x}_L)$ and $\bar{\mathbf{N}}$ are calculated by

$$\tilde{\mathbf{B}}_I^b(\mathbf{x}_L) = \begin{bmatrix} 0 & 0 & 0 & \tilde{b}_{Ix}(\mathbf{x}_L) & 0 \\ 0 & 0 & 0 & 0 & \tilde{b}_{Iy}(\mathbf{x}_L) \\ 0 & 0 & 0 & \tilde{b}_{Iy}(\mathbf{x}_L) & \tilde{b}_{Ix}(\mathbf{x}_L) \end{bmatrix}, \tag{54}$$

$$\tilde{b}_{Ix}(\mathbf{x}_L) = \frac{1}{A_L} \int_{\Gamma_L} \psi_I(\mathbf{x}_L) n_x(x_L) d\Gamma, \quad \tilde{b}_{Iy}(\mathbf{x}_L) = \frac{1}{A_L} \int_{\Gamma_L} \psi_I(\mathbf{x}_L) n_y(x_L) d\Gamma, \tag{55}$$

$$\mathbf{B}_I^b(\mathbf{x}_L) = \begin{bmatrix} 0 & 0 & 0 & \frac{\partial \psi_I(\mathbf{x}_L)}{\partial x} & 0 \\ 0 & 0 & 0 & 0 & \frac{\partial \psi_I(\mathbf{x}_L)}{\partial y} \\ 0 & 0 & 0 & \frac{\partial \psi_I(\mathbf{x}_L)}{\partial y} & \frac{\partial \psi_I(\mathbf{x}_L)}{\partial x} \end{bmatrix}, \tag{56}$$

$$\mathbf{B}_I^m(\mathbf{x}_L) = \begin{bmatrix} \frac{\partial \psi_I(\mathbf{x}_L)}{\partial x} & 0 & 0 & 0 & 0 \\ 0 & \frac{\partial \psi_I(\mathbf{x}_L)}{\partial y} & \frac{\psi_I(\mathbf{x}_L)}{R} & 0 & 0 \\ \frac{\partial \psi_I(\mathbf{x}_L)}{\partial y} & \frac{\partial \psi_I(\mathbf{x}_L)}{\partial x} & 0 & 0 & 0 \end{bmatrix}, \tag{57}$$

$$\mathbf{B}_I^s(\mathbf{x}_L) = \begin{bmatrix} 0 & 0 & \frac{\partial \psi_I(\mathbf{x}_L)}{\partial x} & \psi_I(\mathbf{x}_L) & 0 \\ 0 & 0 & \frac{\partial \psi_I(\mathbf{x}_L)}{\partial y} & 0 & \psi_I(\mathbf{x}_L) \end{bmatrix}, \tag{58}$$

$$\bar{\mathbf{H}} = \begin{bmatrix} \frac{\partial w}{\partial x} & 0 & \frac{\partial w}{\partial y} & 0 & 0 & 0 & 0 & 0 \\ 0 & \frac{\partial w}{\partial y} & \frac{\partial w}{\partial x} & 0 & 0 & 0 & 0 & 0 \end{bmatrix}^T, \tag{59}$$

$$\bar{\mathbf{G}}(\mathbf{x}_L) = \begin{bmatrix} 0 & 0 & \frac{\partial \psi_I(\mathbf{x}_L)}{\partial x} & 0 & 0 \\ 0 & 0 & \frac{\partial \psi_I(\mathbf{x}_L)}{\partial y} & 0 & 0 \end{bmatrix}, \quad \bar{\mathbf{N}} = \begin{bmatrix} N_{xx} & 0 \\ 0 & N_{yy} \end{bmatrix}. \tag{60}$$

3.3. Postbuckling paths

In this section, incremental-iterative Newton-type method combined with the arc-length method is used to solve the non-linear equation system. The governing equation (38) can be re-expressed in incremental form as

$$\mathbf{g}(\mathbf{d}) = \mathbf{K}_s \mathbf{d} - \mathbf{F} = 0, \tag{61}$$

We assume the external load is proportional to a fixed load F_0 as

$$\mathbf{F} = \lambda \mathbf{F}_0, \tag{62}$$

Substituting Eq. (62) into (51), the nonlinear equilibrium equation becomes a function of displacements and the load scaling factor λ

$$\mathbf{g}(\mathbf{d}, \lambda) = \mathbf{K}_s \mathbf{d} - \lambda \mathbf{F}_0 = 0, \tag{63}$$

With the external load changing from λF_0 to $(\lambda + \Delta\lambda)F_0$, we can obtain a new equilibrium configuration near the old configuration

$$\mathbf{g}(\mathbf{d} + \Delta\mathbf{d}, \lambda + \Delta\lambda) = 0, \tag{64}$$

Applying the Taylor series expansion to the above equation,

$$\mathbf{g}(\mathbf{d} + \Delta\mathbf{d}, \lambda + \Delta\lambda) = \mathbf{g}(\mathbf{d}, \lambda) + \mathbf{K}_t \Delta\mathbf{d} - \Delta\lambda \mathbf{F}_0 = 0, \tag{65}$$

The stiffness matrices can be derived from taking the first and second order differential of potential energy with displacements

$$\frac{\partial U}{\partial d_I} = \mathbf{K}_s \mathbf{d}, \tag{66}$$

$$\frac{\partial^2 U}{\partial d_I \partial d_J} = \mathbf{K}_t,$$ (67)

where

$$\mathbf{K}_t = \mathbf{K}_0 + \mathbf{K}_n + \mathbf{K}_G,$$ (68)

where $\mathbf{K}_0$ is the linear stiffness matrix, $\mathbf{K}_G$ is the geometrical stiffness matrix and $\mathbf{K}_n$ is the nonlinear displacement-dependant stiffness matrix.

Thus the incremental formulae of the equilibrium equation and the displacement are given by

$$\Delta\mathbf{d}_m = [\mathbf{K}_t(\mathbf{d}_m)]^{-1}[\Delta\lambda_m\mathbf{F}_0 - \mathbf{g}(\mathbf{d}_m,\lambda_m)] = [\mathbf{K}_t(\mathbf{d}_m)]^{-1}[\Delta\lambda_m\mathbf{F}_0 - \mathbf{K}_s(\mathbf{d}_m)\mathbf{d}_m + \lambda_m\mathbf{F}_0],$$ (69)

$$\mathbf{d}_{m+1} = \mathbf{d}_m + \Delta\mathbf{d}_m,$$ (70)

where m is the load step number.

An additional constraint equation is needed since $\Delta\lambda$ is a new variable to be solved for each incremental step. Here the arc-length continuation is used to provide this constraint. In the arc-length continuation method, subsequent iterations are applied for each $\Delta\lambda$ step to reach a new equilibrium. Superscripts n and m denote the nth iteration cycle and mth load step, respectively. Then the generalized equations of the incremental-iterative formulae are given as

$$\Delta\mathbf{d}_m^n = [(\mathbf{K}_t)_m]^{-1}\left[\Delta\lambda_m^n\mathbf{F}_0 - \mathbf{g}_m^{n-1}\right] = [(\mathbf{K}_t)_m]^{-1}\left[\Delta\lambda_m^n\mathbf{F}_0 - \mathbf{K}_s(\mathbf{d}_m^{n-1})\mathbf{d}_m + \lambda_m^{n-1}\mathbf{F}_0\right] = \Delta\lambda_m^n[\mathbf{d}_f]_m + [\Delta\mathbf{d}_R]_m^n,$$ (71)

$$\mathbf{d}_m^n = \mathbf{d}_m^{n-1} + \Delta\mathbf{d}_m^n,$$ (72)

where $[\mathbf{d}_f]_m$ is one part of the displacement increment from the external load increment and $[\Delta\mathbf{d}_R]_m^n$ is the other one from the residual forces. Here the increment of the load level parameter $\Delta\lambda_m^n$ is obtained by using an iterative arc-length strategy as proposed by Crisfield [39].

The convergence for each iteration process is checked by the following error tolerance procedure:

$$\left\|\mathbf{g}_m^n\right\| \leq \beta\left\|\mathbf{F}_m^n\right\| = \beta\|\leq \lambda_m^n\mathbf{F}_0\|,$$ (73)

where β is a tolerance parameter which is set as 10^{-3}.

4. Numerical results

Postbuckling responses of CNTR-FG cylindrical panels under axial compression are investigated in this section. Poly (methyl methacrylate), referred as PMMA, is selected as the matrix and (10, 10) SWCNTs are selected as reinforcement. The isotropic matrix has material properties $v_m = 0.34$, $\alpha^m = 45(1 + 0.0005\Delta T) \times 10^{-6}/K$ and $E^m = (3.52 - 0.0034T)$ GPa, where $T = T_0 + \Delta T$ and $T_0 = 300$ K (room temperature). Since material properties of SWCNTs are dependent on chirality, size and temperature [40–43], all material properties of SWCNTs used for postbuckling analysis of CNTR-FG cylindrical panels are selected from MD simulation results reported by Zhang and Shen [31]. In this paper, properties of the matrix and CNTs are given as at temperature $T = 300$ K (room temperature), unless otherwise specified. Determining the CNT efficiency parameter is very important for applying the extended rule of mixture to estimate effective material properties of CNTRCs. η_1 is always taken to be 0.2 for short fiber composites [44]. In this paper, CNT efficiency parameters η_1 and η_2 are estimated by matching Young's moduli E_{11} and E_{22} of CNTRCs obtained by the extended rule of mixture to molecular simulation results [45]. As shown in Table 1, the Young's moduli obtained from the extended rule of mixture match very well with those obtained from MD simulation if CNT efficiency parameters η_1 and η_2 are properly chosen. We assume $\eta_3:\eta_2 = 0.7:1$ and $G_{23} = 1.2G_{12} = 1.2G_{13}$ according to [45]. For all cases in this paper, the scaling factor that represents the size of the support is set to be 2.2 and a regular nodal distribution 13×13 is used.

Table 1
Comparison of Young's moduli for PMMA/CNT composites reinforced by (10, 10) SWCNTs under $T = 300$ K (from Shen and Zhang [31]).

V_{CNT}^*	MD [45]		Rule of mixture			
	E_{11} (GPa)	E_{22} (GPa)	E_{11} (GPa)	η_1	E_{22} (GPa)	η_2
0.12	94.6	2.9	94.78	0.137	2.9	1.022
0.17	138.9	4.9	138.68	0.142	4.9	1.626
0.28	224.2	5.5	224.50	0.141	5.5	1.585

4.1. Postbuckling analysis of isotropic cylindrical panel

In this section, postbuckling analysis of an isotropic aluminum cylindrical panel is considered first to validate the present formulations. The material and geometric properties of this aluminum cylindrical panel are Young's modulus $E = 10.0$ Msi, Poisson ratio $\nu = 0.33$, length $a = 14.75$ in, width $b = 14.5$ in., nominal thickness $h = 0.13$ in. and radius $R = 60$ in. In this study, the axial compression loads are assumed to impose only on the curved edges of the panel with the loaded edges clamped and the unloaded edges simply supported. The boundary conditions are defined as

$$\text{Clamped (C) : At } x = 0, \ a : v_0 = w_0 = \phi_x = \phi_y = 0, \tag{74}$$

$$\text{Simply supported (S) : At } y = 0, \ b : w_0 = \phi_x = 0. \tag{75}$$

Fig. 2 shows the central deflection w of the panel subjected to axial compression load $P_b = \tilde{N}_x b$ ($\tilde{N}_x$ is the uniformly distributed load on the curved edges). The corresponding end-shorting response is described in Fig. 3. The results reported by Thornburgh and Hilburger [46] using a finite element method based on Kirchoff–Love thin shell theory and an experimental approach are also provided for comparison. It can be seen that the results obtained by the present element-free method are in reasonable agreement with the solution reported by Thornburgh and Hilburger. Since different shell theories and solution strategies are adopted in these two studies, it can be observed that the buckling point obtained by the proposed method is a little lower than that in the literature.

4.2. Postbuckling analysis of CNTR-FG cylindrical panels

Buckling analysis for CNTR-FG cylindrical panels is carried out in which the first four buckling mode shapes of FG-X cylindrical panel are obtained and presented in Fig. 4. It follows by a parametric study to investigate the postbuckling response of CNTR-FG cylindrical panels under axial compression. In this section, the effects of CNT volume fraction, length-to-thickness ratio and radius on postbuckling behaviors of CNTR-FG cylindrical panels are examined in detail. Also, different types of distributions of CNTs in the cylindrical panels and two more boundary conditions are considered. The external axial compression loads are also assumed to impose only on the curved edges. The non-dimensional parameters including a central deflection $\bar{w} = w/h$, end-shorting $\bar{u} = u/h$ and load parameter $N_b = \tilde{N}_x a^2 / E_m h^3$ are defined to report the results and typical results are shown in Figs. 5–18.

Figs. 5 and 6 show the non-dimensional central deflection and end-shorting of various types of CNTR-FG cylindrical panels under axial compression. Geometric properties of the panel are $a = b = 0.2$ m, $\theta_0 = 0.2$ rad, $R = 1.0$ m and $h = 0.004$ m. The CNT volume fraction V_{CNT}^* is taken to be 0.12. It can be seen that the central deflection increases slowly in the pre-buckling stage and increases very fast in the postbuckling stage. We also find that there are no apparent buckling points, although the central deflection increases relatively quickly in the mid-stage between the pre-buckling and postbuckling stages. For end-shorting in the pre-buckling and postbuckling stages, the relationship of displacement and the load parameter is almost linear. For different types of distributions of SWCNT in the cylindrical panels, it can be seen that FG-O cylindrical panel has the lowest postbuckling strength, while FG-X cylindrical panel has the highest postbuckling strength among the three types of CNTR-FG cylindrical panels, and the postbuckling path of UD cylindrical panel lies between FG-X and FG-O. It is concluded
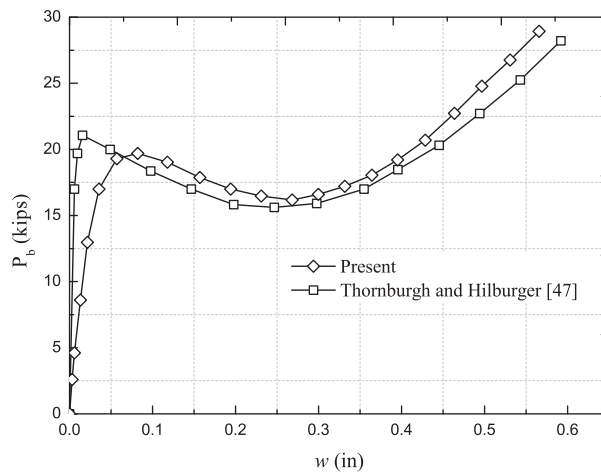

Fig. 2. The central deflection of a curved isotropic aluminum panel under axial compression with CCSS boundary conditions ($a = 14.75$ in, $b = 14.5$ in, $h = 0.13$ in, $R = 60$ in).
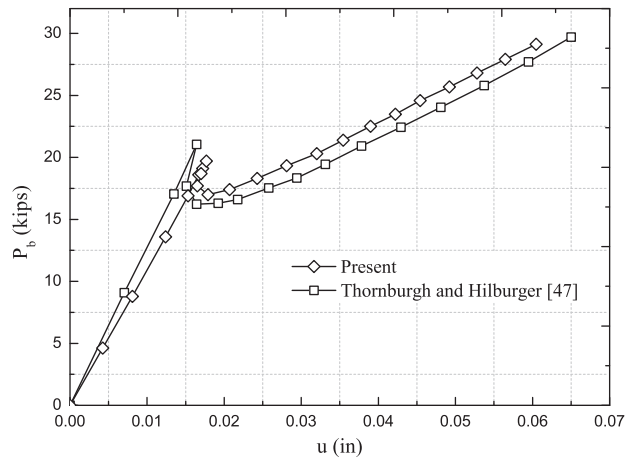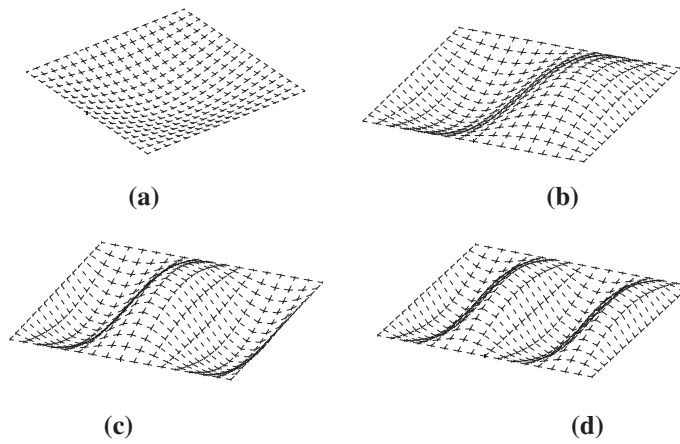
Fig. 3. The end shorting of a curved isotropic aluminum panel under axial compression with CCSS boundary conditions (a = 14.75 in, b = 14.5 in, h = 0.13 in, R = 60 in).

(a) **(b)**

(c) **(d)**

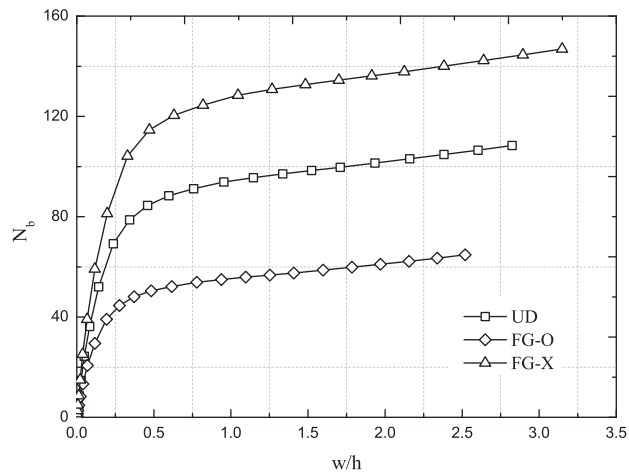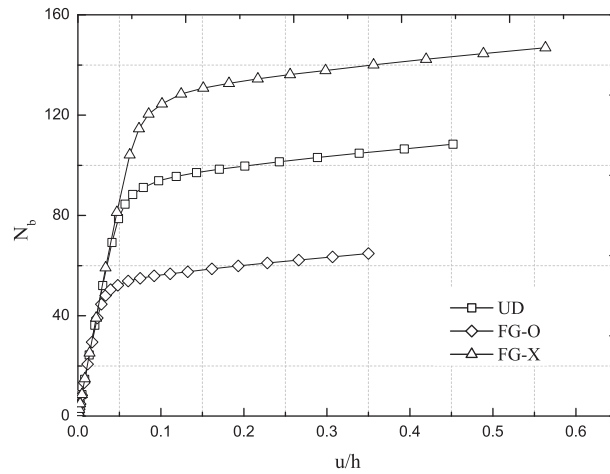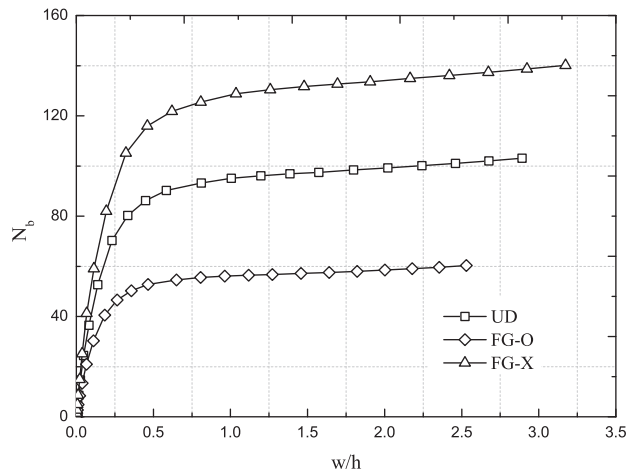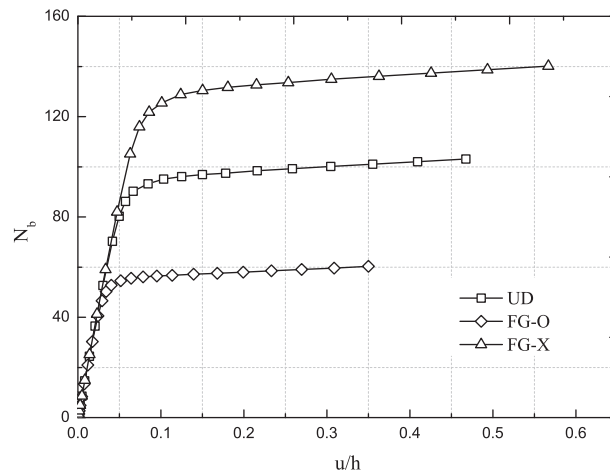**Fig. 4.** The first four buckling mode shapes of FG-X cylindrical panel.

Fig. 5. The non-dimensional central deflection of FG-CNTRC cylindrical panels under axial compression with CCSS boundary conditions (a = b = 0.2 m, θ_0 = 0.2 rad, R = 1.0 m, h = 0.004 m, $V_{CNT}^* = 0.12$).

Fig. 6. The non-dimensional end shorting of FG-CNTRC cylindrical panels under axial compression with CCSS boundary conditions ($a = b = 0.2$ m, $\theta_0 = 0.2$ rad, $R = 1.0$ m, $h = 0.004$ m, $V^*_{CNT} = 0.12$).
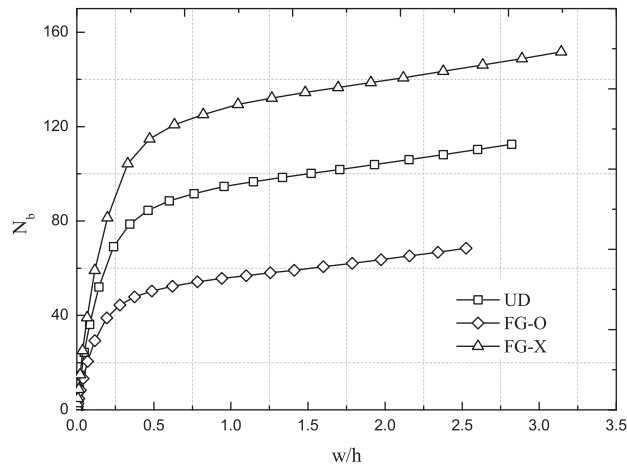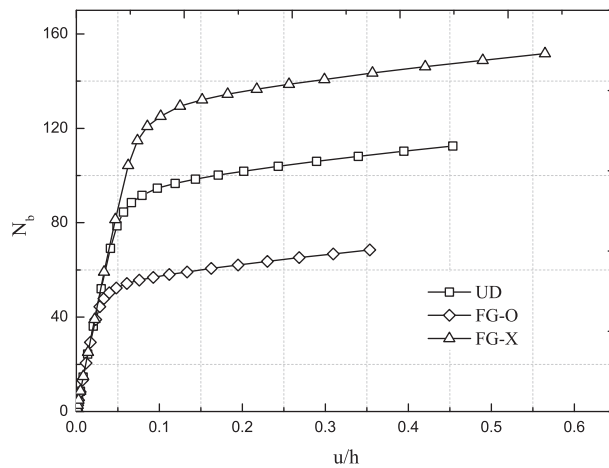

Fig. 7. The non-dimensional central deflection of FG-CNTRC cylindrical panels under axial compression with CCSS boundary conditions ($a = b = 0.2$ m, $\theta_0 = 0.2$ rad, $R = 0.5$ m, $h = 0.004$ m, $V^*_{CNT} = 0.12$).

Fig. 8. The non-dimensional end shorting of FG-CNTRC cylindrical panels under axial compression with CCSS boundary conditions ($a = b = 0.2$ m, $\theta_0 = 0.2$ rad, $R = 0.5$ m, $h = 0.004$ m, $V^*_{CNT} = 0.12$).
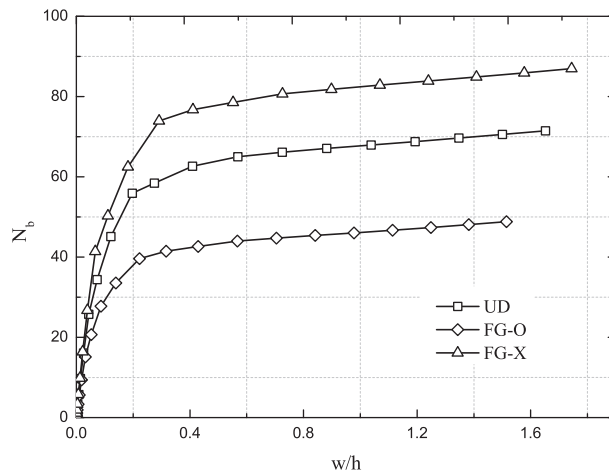
Fig. 9. The non-dimensional central deflection of FG-CNTRC cylindrical panels under axial compression with CCSS boundary conditions ($a = b = 0.2$ m, $\theta_0 = 0.2$ rad, $R = 2.0$ m, $h = 0.004$ m, $V_{CNT}^* = 0.12$).
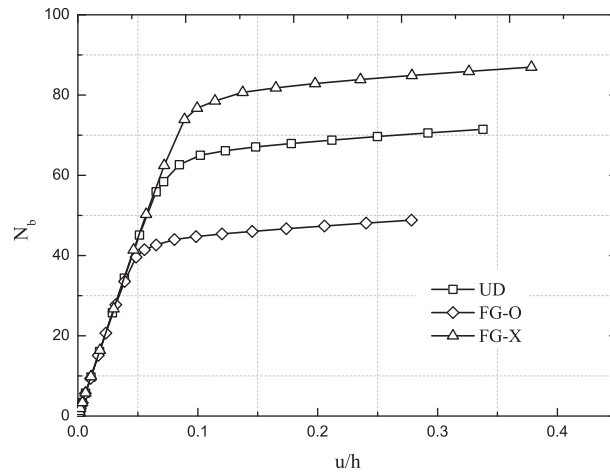

Fig. 10. The non-dimensional end shorting of FG-CNTRC cylindrical panels under axial compression with CCSS boundary conditions ($a = b = 0.2$ m, $\theta_0 = 0.2$ rad, $R = 2.0$ m, $h = 0.004$ m, $V_{CNT}^* = 0.12$).

Fig. 11. The non-dimensional central deflection of FG-CNTRC cylindrical panels under axial compression with CCSS boundary conditions ($a = b = 0.2$ m, $\theta_0 = 0.2$ rad, $R = 1.0$ m, $h = 0.008$ m, $V_{CNT}^* = 0.12$).
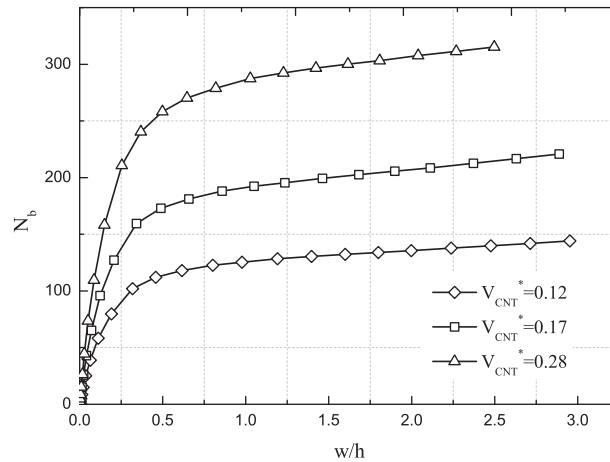
Fig. 12. The non-dimensional end shorting of FG-CNTRC cylindrical panels under axial compression with CCSS boundary conditions ($a = b = 0.2$ m, $\theta_0 = 0.2$ rad, $R = 1.0$ m, $h = 0.008$ m, $V_{CNT}^* = 0.12$).

Fig. 13. Effect of CNT volume fraction on the central deflection of a FG-X CNTRC cylindrical panel under axial compression with CCSS boundary conditions ($a = b = 0.2$ m, $\theta_0 = 0.2$ rad, $R = 1.0$ m, $h = 0.004$ m).
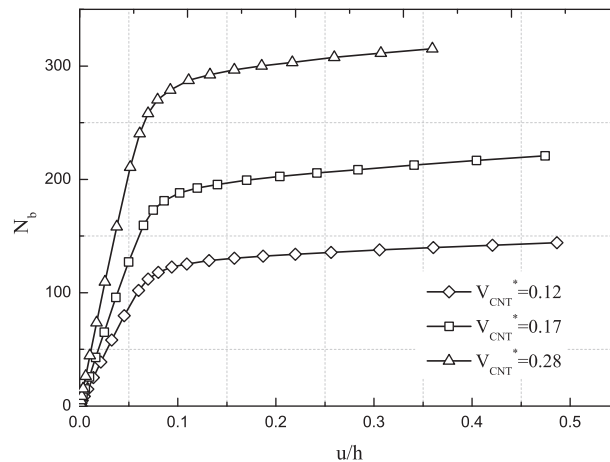

Fig. 14. Effect of CNT volume fraction on the end shorting of a FG-X CNTRC cylindrical panel under axial compression with CCSS boundary conditions ($a = b = 0.2$ m, $\theta_0 = 0.2$ rad, $R = 1.0$ m, $h = 0.004$ m).
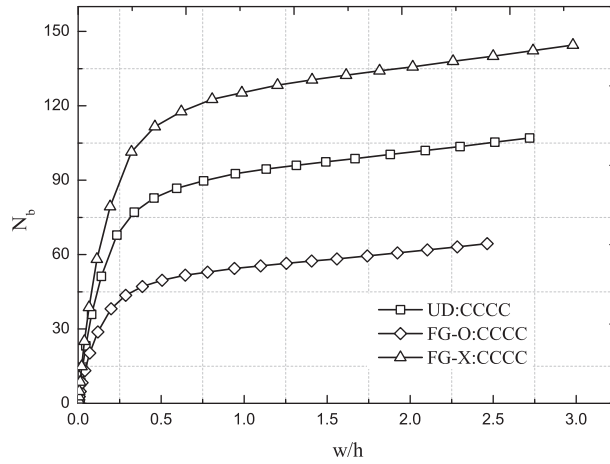
Fig. 15. The non-dimensional central deflection of FG-CNTRC cylindrical panels under axial compression with CCCC boundary conditions ($a = b = 0.2$ m, $\theta_0 = 0.2$ rad, $R = 1.0$ m, $h = 0.004$ m, $V_{CNT}^* = 0.12$).
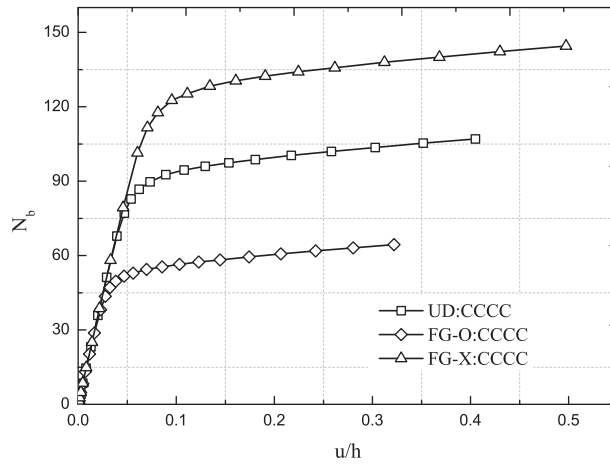

Fig. 16. The non-dimensional end shorting of FG-CNTRC cylindrical panels under axial compression with CCCC boundary conditions ($a = b = 0.2$ m, $\theta_0 = 0.2$ rad, $R = 1.0$ m, $h = 0.004$ m, $V_{CNT}^* = 0.12$).
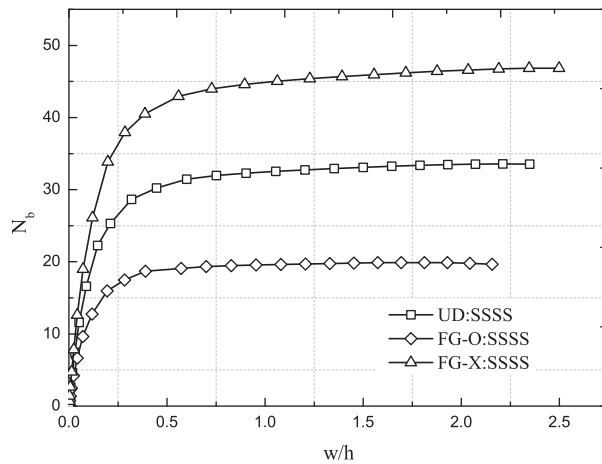

Fig. 17. The non-dimensional central deflection of FG-CNTRC cylindrical panels under axial compression with SSSS boundary conditions ($a = b = 0.2$ m, $\theta_0 = 0.2$ rad, $R = 1.0$ m, $h = 0.004$ m, $V_{CNT}^* = 0.12$).
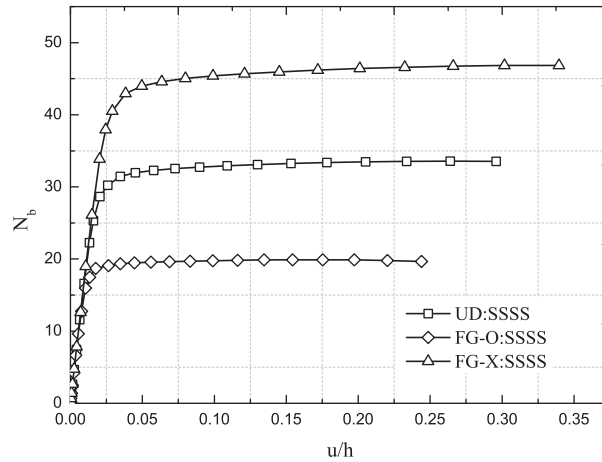
Fig. 18. The non-dimensional end shorting of FG-CNTRC cylindrical panels under axial compression with SSSS boundary conditions ($a = b = 0.2$ m, $\theta_0 = 0.2$ rad, $R = 1.0$ m, $h = 0.004$ m, $V_{CNT}^* = 0.12$).

that CNTs distributed close to top and bottom surfaces are more efficient in increasing the stiffness and postbuckling strength of the CNTR-FG cylindrical panels than CNTs distributed near the mid-plane.

Subsequently, CNTR-FG cylindrical panels with two different radii $R = 0.5$ m and $R = 2.0$ m are considered. The effect of radii of cylindrical panels on the postbuckling behavior is studied. As shown in Figs. 7–10, it can be seen that the change of radius of CNTR-FG cylindrical panels has little effect on the postbuckling behavior of CNTR-FG cylindrical panels. With the radius of cylindrical panels changing from 0.5 to 2.0, the postbuckling strength is slightly decreased. We have also observed that the slope of the postbuckling curves in the postbuckling stage is slightly increased with the increases of the radius of CNTR-FG cylindrical panels.

Fig. 11 shows the non-dimensional central deflection of thicker CNTR-FG cylindrical panels ($h = 0.008$ m) under axial compression. The corresponding end-shorting response is depicted in Fig. 12. It can be seen that the trends of the non-dimensional central deflection and end-shorting are similar to those in Figs. 5 and 6. The result also confirms that thicker CNTR-FG cylindrical panels have higher postbuckling strength. Compared with results in Figs. 5 and 6, a similar effect of the distribution types of CNTs in the cylindrical panels can also obtained.

Figs. 13 and 14 show the non-dimensional central deflection and end-shorting of a FG-X CNTRC cylindrical panel under axial compression with different values of CNT volume fraction ($a = b = 0.2$ m, $\theta_0 = 0.2$ rad, $R = 1.0$ m, $h = 0.004$ m). It can be seen that the larger the carbon nanotube volume fraction, the greater is the degree of postbuckling strength observed. This is to be expected, because the increase of the carbon nanotube volume fraction yields an increase of postbuckling strength and the CNTR-FG cylindrical panel becomes stiffer.

To check the effect of boundary conditions on postbuckling behavior of FG-CNTRC cylindrical panels, two more boundary conditions, namely, simply supported (SSSS) and four edges fully clamped (CCCC), are considered in addition to the CCSS boundary condition.

In this study, the boundary conditions are defined as:

For simply supported edge (S):

at $x = 0,\ a : v_0 = w_0 = \phi_y = 0,$

at $y = 0,\ b : u_0 = w_0 = \phi_x = 0.$

For clamped edge (C):

at $x = 0,\ a : v_0 = w_0 = \phi_x = \phi_y = 0,$

at $y = 0,\ b : u_0 = w_0 = \phi_x = \phi_y = 0.$

As shown in Figs. 15 and 16, it can be seen that changing the boundary condition of the unloaded edges has a little effect on postbuckling behavior of CNTR-FG cylindrical panels. However, when we change the boundary condition of the loaded curved edges of the panel from clamped (C) to simply supported (S), the postbuckling strength of CNTR-FG cylindrical panels decreases very quickly (Figs. 17 and 18). It is concluded that the boundary condition of the loaded curved edges of the panel has a pronounced effect on the postbuckling response of CNTR-FG cylindrical panels.

5. Conclusions

This paper presents a postbuckling analysis of various types of CNTR-FG cylindrical panels, using the element-free *kp*-Ritz method combined with the first order shear deformation shell theory and von Kármán strains. The CNTs are assumed to be graded in the thickness direction which is symmetric about the middle surface of the cylindrical panel. The effective material properties of CNTR-FG cylindrical panels are estimated through a micromechanical model based on the extended rule of mixture. For eliminating shear locking, a stabilized conforming nodal integration method and direct nodal integration are employed to evaluate stiffness matrices of cylindrical panels. The postbuckling governing equations are solved by a combination of the arc-length iterative algorithm and the modified Newton–Raphson method to trace the postbuckling path of CNTR-FG cylindrical panels. Several numerical cases are used for study of the effect of various parameters including the carbon nanotube volume fraction, length-to-thickness ratio and radius on the postbuckling behavior of CNTR-FG cylindrical panels. The effects of boundary conditions and distribution types of CNTs in the cylindrical panels are also studied.

Acknowledgement

References

[1] E.T. Thostenson, C. Li, T.W. Chou, Nanocomposites in context, Compos. Sci. Technol. 65 (2005) 491–516.
[2] A.K.T. Lau, D. Hui, The revolutionary creation of new advanced materials-carbon nanotube composites, Compos. Part B 33 (2002) 263–277.
[3] P.J.F. Harris, Carbon Nanotubes and Related Structures: New Materials for the Twenty-First Century, Cambridge University Press, 2001.
[4] C.H. Sun, F. Li, H.M. Cheng, G.Q. Lu, Axial Young's modulus prediction of single-walled carbon nanotube arrays with diameters from nanometer to meter scales, Appl. Phys. Lett. 87 (2005) 193101–193103.
[5] J.N. Coleman, U. Khan, W.J. Blau, Y.K. Gun'ko, Small but strong: a review of the mechanical properties of carbon nanotube-polymer composites, Carbon 44 (2006) 1624–1652.
[6] D. Qian, E.C. Dickey, R. Andrews, T. Rantell, Load transfer and deformation mechanisms in carbon nanotube-polystyrene composites, Appl. Phys. Lett. 76 (2000) 2868–2870.
[7] F.H. Gojny, M.H.G. Wichmann, B. Fiedler, K. Schulte, Influence of different carbon nanotubes on the mechanical properties of epoxy matrix composites-A comparative study, Compos. Sci. Technol. 65 (2005) 2300–2313.
[8] P. Pötschke, T.D. Fornes, D.R. Paul, Rheological behavior of multiwalled carbon nanotube/polycarbonate composites, Polymer 43 (2002) 3247–3255.
[9] J.D. Fidelus, E. Wiesel, F.H. Gojny, K. Schulte, H.D. Wagner, Thermo-mechanical properties of randomly oriented carbon/epoxy nanocomposites, Compos. Part A 36 (2005) 1555–1561.
[10] J. Wuite, S. Adali, Deflection and stress behaviour of nanocomposite reinforced beams using a multiscale analysis, Compos. Struct. 71 (2005) 388–396.
[11] T. Vodenitcharova, L.C. Zhang, Bending and local buckling of a nanocomposite beam reinforced by a single-walled carbon nanotube, Int. J. Solids Struct. 43 (2006) 3006–3024.
[12] M.H. Yas, N. Samadi, Free vibrations and buckling analysis of carbon nanotube-reinforced composite Timoshenko beams on elastic foundation, Int. J. Press. Ves. Pip. 98 (2012) 119–128.
[13] P. Zhu, Z.X. Lei, K.M. Liew, Static and free vibration analyses of carbon nanotube-reinforced composite plates using finite element method with first order shear deformation plate theory, Compos. Struct. 94 (2012) 1450–1460.
[14] H.S. Shen, Nonlinear bending of functionally graded carbon nanotube-reinforced composite plates in thermal environments, Compos. Struct. 91 (2009) 9–19.
[15] Z.X. Wang, H.S. Shen, Nonlinear vibration of nanotube-reinforced composite plates in thermal environments, Comput. Mater. Sci. 50 (2011) 2319–2330.
[16] S.J. Mehrabadi, B.S. Aragh, V. Khoshkhahesh, A. Taherpour, Mechanical buckling of nanocomposite rectangular plate reinforced by aligned and straight single-walled carbon nanotubes, Compos. Part B 43 (2012) 2031–2040.
[17] H.S. Shen, Y. Xiang, Nonlinear vibration of nanotube-reinforced composite cylindrical shells in thermal environments, Comput. Methods. Appl. Mech. Engrg. 213–216 (2012) 196–205.
[18] B.S. Aragh, A.H.N. Barati, H. Hedayati, Eshelby–Mori–Tanaka approach for vibrational behavior of continuously graded carbon nanotube-reinforced cylindrical panels, Compos. Part B 43 (2012) 1943–1954.
[19] H.S. Shen, Thermal buckling and postbuckling behavior of functionally graded carbon nanotube-reinforced composite cylindrical shells, Compos. Part B 43 (2012) 1030–1038.
[20] H.S. Shen, Postbuckling of nanotube-reinforced composite cylindrical shells in thermal environments. Part I: Axially-loaded shells, Compos. Struct. 93 (2011) 2096–2108.
[21] H.S. Shen, Postbuckling of nanotube-reinforced composite cylindrical shells in thermal environments. Part II: Pressure-loaded shells, Compos. Struct. 93 (2011) 2496–2503.
[22] Z.X. Lei, K.M. Liew, J.L. Yu, Buckling analysis of functionally graded carbon nanotube-reinforced composite plates using the element-free *kp*-Ritz method, Compos. Struct. 98 (2013) 160–168.
[23] Z.X. Lei, K.M. Liew, J.L. Yu, Large deflection analysis of functionally graded carbon nanotube-reinforced composite plates by the element-free *kp*-Ritz method, Comput. Methods. Appl. Mech. Engrg. 256 (2013) 189–199.
[24] X. Li, H. Gao, W.A. Scrivens, D. Fei, X. Xu, M.A. Sutton, A.P. Reynolds, M.L. Myrick, Reinforcing mechanisms of single-walled carbon nanotube-reinforced polymer composites, J. Nanosci. Nanotechnol. 7 (2007) 2309–2317.
[25] A.M.K. Esawi, M.M. Farag, Carbon nanotube reinforced composites: potential and current challenges, Mater. Des. 28 (2007) 2394–2401.
[26] G.D. Seidel, D.C. Lagoudas, Micromechanical analysis of the effective elastic properties of carbon nanotube reinforced composites, Mech. Mater. 38 (2006) 884–907.
[27] V. Anumandla, R.F. Gibson, A comprehensive closed form micromechanics model for estimating the elastic modulus of nanotube-reinforced composites, Compos. Part A 37 (2006) 2178–2185.
[28] B. Sobhani Aragh, A.H. Nasrollah Barati, H. Hedayati, Eshelby–Mori–Tanaka approach for vibrational behavior of continuously graded carbon nanotube-reinforced cylindrical panels, Compos. Part B 43 (2012) 1943–1954.
[29] G. Formica, W. Lacarbonara, R. Alessi, Vibrations of carbon nanotube-reinforced composites, J. Sound Vib. 329 (2010) 1875–1889.
[30] J. Wang, R. Pyrz, Prediction of the overall moduli of layered silicate-reinforced nanocomposites. Part I: Basic theory and formulas, Compos. Sci. Technol. 64 (2004) 925–934.

[31] H.S. Shen, C.L. Zhang, Thermal buckling and postbuckling behavior of functionally graded carbon nanotube-reinforced composite plates, Mater. Des. 31 (2010) 3403–3411.

[32] L. Librescu, S.Y. Oh, O. Song, Thin-walled beams made of functionally graded materials and operating in a high temperature environment: vibration and stability, J. Therm. Stress. 28 (2005) 649–712.

[33] J.N. Reddy, Mechanics of Laminated Composite Plates and Shells: Theory and Analysis, second ed., CRC Press, Boca Raton, FL, 2004.

[34] J.S. Chen, C. Pan, C.T. Wu, W.K. Liu, Reproducing kernel particle methods for large deformation analysis of non-linear structures, Comput. Methods. Appl. Mech. Engrg. 139 (1996) 195–227.

[35] W.K. Liu, S. Jun, Y.F. Zhang, Reproducing kernel particle methods, Int. J. Numer. Methods Fluids 20 (1995) 1081–1106.

[36] J.S. Chen, C.T. Wu, S. Yoon, Y. You, A stabilized conforming nodal integration for Galerkin mesh-free methods, Int. J. Numer. Methods Engrg. 50 (2001) 435–466.

[37] J. Dolbow, T. Belytschko, Numerical integration of the Galerkin weak form in meshfree methods, Comput. Mech. 23 (1999) 219–230.

[38] S. Beissel, T. Belytschko, Nodal integration of the element-free Galerkin method, Comput. Methods. Appl. Mech. Engrg. 139 (1996) 49–74.

[39] M.A. Crisfield, Nonlinear Finite Element Analysis of Solids and Structures, John Wiley & Sons, Chichester, UK, 1991.

[40] T.C. Chang, J.Y. Geng, X.M. Guo, Chirality- and size-dependent elastic properties of single-walled carbon nanotubes, Appl. Phys. Lett. 87 (2005).

[41] J.A. Elliott, J.K.W. Sandler, A.H. Windle, R.J. Young, M.S.P. Shaffer, Collapse of single-wall carbon nanotubes is diameter dependent, Phys. Rev. Lett. 92 (2004) 095501.

[42] Y. Jin, F.G. Yuan, Simulation of elastic properties of single-walled carbon nanotubes, Compos. Sci. Technol. 63 (2003) 1507–1515.

[43] K.M. Liew, J.W. Yan, Y.Z. Sun, L.H. He, Investigation of temperature effect on the mechanical properties of single-walled carbon nanotubes, Compos. Struct. 93 (2011) 2208–2212.

[44] H. Fukuda, K. Kawata, On Young's modulus of short fibre composites, Fibre Sci. Technol. 7 (1974) 207–222.

[45] Y. Han, J. Elliott, Molecular dynamics simulations of the elastic properties of polymer/carbon nanotube composites, Comput. Mater. Sci. 39 (2007) 315–323.

[46] R.P. Thornburgh, M.W. Hilburger, Identifying and characterizing discrepancies between test and analysis results of compression-loaded panels, NASA/TM-2005-213932, ARL-TR-3664.